

Article

Super-Fast Sodium Storage Properties of Nitrogen-Doped Graphene-Based Material Synthesized via Arc-Discharge Method

Injun Jeon ^{1,2}, Chunghun Kim ³, Minseung Kang ¹, Hyun Woo Kim ¹ , Hong Chen ¹, Hye Seon Youn ¹, Myung Jong Kim ^{3,*} and Chae-Ryong Cho ^{1,4,*} 

¹ Department of Nano Fusion Technology, Pusan National University, Busan 46241, Republic of Korea; iujeon@dgist.ac.kr (I.J.); twomin0000@pusan.ac.kr (M.K.); kimhw0425@pusan.ac.kr (H.W.K.); chenhong4819@pusan.ac.kr (H.C.); yhs0723@pusan.ac.kr (H.S.Y.)

² Division of Energy & Environmental Technology, Daegu Gyeongbuk Institute of Science & Technology (DGIST), Daegu 42988, Republic of Korea

³ Department of Chemistry, Gachon University, Seongnam 13120, Republic of Korea; kimchunghun@gachon.ac.kr

⁴ Department of Nanoenergy Engineering, Pusan National University, Busan 46241, Republic of Korea

* Correspondence: myungjongkim@gachon.ac.kr (M.J.K.); crcho@pusan.ac.kr (C.-R.C.);

Tel.: +82-31-750-8721 (M.J.K.); +82-51-510-6114 (C.-R.C.)

Abstract: We investigated the electrochemical performance of undoped artificial graphene-based material (UAG) and N-doped graphene-based material (NAG, ~3.5% nitrogen doping), synthesized by the arc-discharge method, for sodium-ion battery anodes. The NAG demonstrated slightly superior fast-charging capability compared to UAG, achieving a specific capacity of 46.8 mAh g^{-1} at 30 A g^{-1} , compared to UAG's capacity of 36.7 mAh g^{-1} , representing an enhancement of approximately 28%. It also showed high cycle stability, retaining a capacity of 100 mAh g^{-1} (retention ratio ~99.9%) after 2500 cycles at 5 A g^{-1} , compared to UAG's retention of 90 mAh g^{-1} (retention ratio ~95%). The diffusion behavior of the UAG and NAG samples was significantly higher than that of graphite. The improvement in electrochemical properties is attributed to the successful doping of nitrogen in NAG, which results in enhanced electrical conductivity and structural disordering.



Academic Editor: Dongliang Chao

Received: 1 February 2025

Revised: 21 March 2025

Accepted: 27 March 2025

Published: 29 March 2025

Citation: Jeon, I.; Kim, C.; Kang, M.; Kim, H.W.; Chen, H.; Youn, H.S.; Kim, M.J.; Cho, C.-R. Super-Fast Sodium Storage Properties of Nitrogen-Doped Graphene-Based Material Synthesized via Arc-Discharge Method. *Batteries* **2025**, *11*, 135. <https://doi.org/10.3390/batteries11040135>

Copyright: © 2025 by the authors. Licensee MDPI, Basel, Switzerland. This article is an open access article distributed under the terms and conditions of the Creative Commons Attribution (CC BY) license (<https://creativecommons.org/licenses/by/4.0/>).

1. Introduction

Recently, with the exponential proliferation of lithium-ion batteries (LIBs) in portable electronics, electric vehicles, and mobility applications, significant advancements have been made in the development of materials for battery cathodes, anodes, and electrolytes [1,2]. Concurrently, the global demand for resources such as lithium, nickel, cobalt, and iron has surged, leading to issues such as resource monopolization by certain countries and soaring prices [3]. As a result, extensive research is being conducted into alternative metal-ion batteries, including sodium [4–6], potassium [7,8], aluminum [9], and zinc-ion batteries [10]. Among these, sodium-ion batteries (SIBs) are emerging as a promising alternative to LIBs. Although sodium ions have larger ionic radii and greater atomic mass compared to lithium ions, resulting in lower energy density, they possess a relatively high reduction potential (−2.74 V versus the standard hydrogen electrode) and allow for the use of aluminum as

an anode current collector [11]. Moreover, the abundant availability of sodium makes it a highly competitive alternative resource [12].

SIBs face significant challenges when using sodium metal as the anode due to its high theoretical capacity of 1165 mAh g⁻¹. Like LIBs, SIBs are susceptible to active side reactions at the electrode and the growth of sodium dendrites, both of which impede the battery's lifespan and raise safety concerns [13–16]. These issues can be mitigated by using alternative anode materials capable of intercalating, inserting, or alloying sodium ions, such as carbon [17–21], oxides [22–27], and sulfides [28–30]. Among these, carbon materials are the most well-known and commonly used anode materials for sodium-ion batteries due to their ease of synthesis or extraction and cost-effectiveness.

Graphite, a widely used anode material in LIBs, can intercalate one lithium ion per six carbon atoms (372 mAh g⁻¹, LiC₆) [31]. However, in graphite as SIB anodes, sodium ions require co-intercalation with solvents in ether-based electrolytes for efficient storage, making electrolyte selection crucial and posing limitations on sodium storage performance [21,32,33]. Additionally, the bulky nature of graphite limits sodium diffusion, which is detrimental to high-rate charging [34,35]. To address these limitations, various methods have been explored to enhance sodium intercalation, such as introducing defects in ordered layered structures, using defect-rich graphene or graphite, or employing disordered hard carbons [36–38].

Graphene, a carbon material with a graphitized structure, has attracted significant attention as a promising anode material due to its large specific surface area and exceptional electrical properties, which stem from its unique two-dimensional architecture. The charging rate and cycle life of graphene-based anodes are strongly influenced by ion mobility within the internal and surface regions of the material. The electrochemical performance of graphene anodes can be further enhanced through strategies such as introducing internal defects, doping with heteroatoms, and modifying particle morphology. Electrochemical analysis of various graphene-based materials prepared by chemical methods for use as active materials in secondary batteries has been extensively conducted [39–42]. N-doped graphene has been used to improve its electrochemical performance through both chemical and physical methods. However, the large-scale production of N-doped graphene remains a significant challenge due to process-related limitations, and optimizing its structural and chemical properties often requires additional, resource-intensive processing steps.

In this study, we present graphene-based materials synthesized via a facile method to create a turbostratic structure and demonstrate their application as anode material for sodium-ion batteries. The arc discharge synthesis method for graphene-based materials is a straightforward and scalable approach for producing high-quality graphitized carbon. It involves applying a high voltage between carbon-based electrodes to generate high-temperature plasma, which facilitates the formation of artificial graphene-based powder materials. This method also enables the easy incorporation of impurities during the arc discharge process, making it an effective technique for synthesizing graphene doped with heteroatoms. The undoped and nitrogen-doped artificial graphene material in this study exhibits promising electrochemical performance due to its unique structure, which provides enhanced sodium ion storage capabilities and improved cycling stability. Despite its low specific surface area, the artificial graphene-based material has demonstrated higher sodium storage capacity and longevity compared to graphite at elevated charging currents. The increased sodiation rate is attributed to the rapid sodium ion diffusion within the internal layers of the turbostratic structure, suggesting its potential application as a high-speed charging anode material for sodium-ion batteries.

2. Methods

2.1. Preparation of Artificial Graphene-Based Materials

The synthesis of artificial graphene-based materials was performed using the arc-discharge method as illustrated in Figure S1, following protocols established in prior studies [43,44]. Commercial graphite powder (50 μm , Kojndo Korea Co., Ltd., Uiwang, Republic of Korea), graphene oxide (approximately 40 at% oxygen, Standard Graphene, Ulsan, Republic of Korea), and polyaniline (PANI, $M_w \sim 20,000$, MilliporeSigma, Burlington, MA, USA) were employed as carbon feedstock materials, with their proportions optimized for the arc-discharge process. For the nitrogen-doped artificial graphene-based materials (NAG) synthesis, a precursor mixture comprising graphite, graphene oxide, and PANI in a mass ratio of 2:1:1 was prepared. This mixture was placed in a chamber evacuated to 5×10^{-2} Torr and subsequently filled with a gas mixture of helium (400 sccm), hydrogen (100 sccm), and ammonia (400 sccm). The arc-discharge process was conducted under dynamic pumping to maintain a chamber pressure of 550 Torr, with the voltage and current set to 30 V and 150 A, respectively. The synthesis of undoped artificial graphene-based materials (UAG) followed an identical procedure to that of NAG, except that graphite was used as the sole feedstock material. The process employed a gas mixture of helium (400 sccm) and hydrogen (400 sccm) at the same operational parameters.

2.2. Material Characterization

The surface morphology of the prepared samples (artificial graphite, UAG, and NAG) was analyzed using field-emission scanning electron microscopy (FE-SEM, S4800, Hitachi, Tokyo, Japan). Their internal structures were examined in detail with a 300 kV high-resolution transmission electron microscope (HR-TEM, Themis Z, Thermo Fisher Scientific, Waltham, MA, USA). Structural characteristics were further investigated via powder X-ray diffraction (XRD, Empyrean, PANalytical, Almelo, The Netherlands), while the degree of graphitization and internal defect states were assessed by fitting spectra obtained from high-resolution Raman spectroscopy (inVia Qontor, Renishaw, Wotton-under-Edge, United Kingdom) with a 532 nm laser wavelength, with artificial graphite serving as a reference. The chemical bonding states of the synthesized active materials after Ar^+ ion sputtering during 100 s were characterized using X-ray photoelectron spectroscopy (XPS, K-Alpha, Thermo Fisher Scientific, Waltham, MA, USA) with Al K_α radiation. The three carbon materials (graphite, UAG, and NAG) were sandwiched between stainless steel (SS) plates, and their impedance values were measured to compare electrical resistivity.

2.3. Electrochemical Properties

To evaluate the electrochemical properties of UAG and NAG as anode materials for sodium-ion batteries, half-cells were constructed using sodium metal as both the counter and reference electrode. The working electrode consisted of either UAG or NAG as the active materials. Sodium metal foil (99.95%, MilliporeSigma, Burlington, MA, USA) was used as the counter and reference electrode, while a borosilicate microfiber filter (GF/A, Whatman, Maidstone, United Kingdom) served as the separator. The electrolyte solution was prepared using 1 M NaPF_6 in diethylene glycol dimethyl ether (DEGDME).

The working electrodes were fabricated by mixing 80 wt% active material (UAG or NAG), 10 wt% acetylene black (MTI Korea, Sungnam, Republic of Korea) as a conductive additive, and 10 wt% SBR/CMC (MTI Korea, Sungnam, Republic of Korea) binder in a 1:1 weight ratio. This mixture was then cast onto a copper current collector and dried thoroughly before assembling the half-cell. Electrochemical tests (WBCS3000Le32, Wonatech, Seoul, Republic of Korea) were conducted to evaluate the performance of the prepared anode materials. These included cyclic voltammetry (CV) to analyze the redox behavior

and Na^+ insertion/extraction kinetics, galvanostatic charge/discharge cycling to assess specific capacity and cycling stability, and diffusivity of the anode materials were measured by using galvanostatic intermittent titration technique (GITT). Furthermore, in situ electrochemical impedance spectroscopy (EIS, MP1, Wonatech, Seoul, Republic of Korea) was performed to characterize the electrochemical impedance of the prepared anode materials by fitting Nyquist plots as a function of cell potential. For comparative purposes, artificial graphite (SCMG-BH, Resonac, Tokyo, Japan) electrodes were fabricated following the same preparation process to evaluate electrochemical performance relative to arc-discharge graphene-based materials.

3. Results and Discussion

Figure 1 shows surface images and structural data for the graphite, UAG, and NAG samples. Figure 1a–f presents the SEM images of commercial artificial graphite and arc-discharged UAG and NAG samples. The SEM images reveal a wrinkled surface morphology for UAG synthesized through arc discharge, as shown in Figure 1c,d. Additionally, NAG, which was synthesized with the addition of PANI for nitrogen doping, as presented in Figure 1e,f, exhibits a similar surface morphology to UAG. Figure 1g presents the XRD patterns of the three samples. The (002) peaks for UAG and NAG are observed at 26.7° [$d_{002} = 3.333 \text{ \AA}$] and 26.6° [$d_{002} = 3.347 \text{ \AA}$], respectively, indicating an increased interlayer spacing due to nitrogen doping. Broad peaks are also observed at 26.2° [$d_{ts} = 3.405 \text{ \AA}$] for UAG and 26.1° [$d_{ts} = 3.410 \text{ \AA}$] for NAG, characteristic of a typical turbostratic structure. This suggests the presence of numerous defects and atomic pores within the material (Table S1). Figure 1h shows the Raman spectra of graphite, UAG, and NAG, with D peaks at 1390 cm^{-1} and G peaks at 1590 cm^{-1} . The 2D peak, indicative of an ordered graphitic structure, is also observed at 2750 cm^{-1} . In contrast to graphite or ordered graphene, turbostratic structure is expected to facilitate rapid charge/discharge cycles by providing additional ion diffusion pathways through its internal pores and defects. To compare defects and ordering in the graphitic structures across the three samples, the Raman spectra of the D and G bands were deconvoluted in detail by using the Gaussian function, as shown in Figure 1i and Table S2. In detail, the Raman spectrum of a graphitic carbon containing defects or disorder can be deconvoluted into D1 (around 1350 cm^{-1}), D2 (around 1605 cm^{-1}), D3 (around 1500 cm^{-1}), D4 (around 1175 cm^{-1}), and G (around 1590 cm^{-1}) bands. Each component of the bands corresponds to different vibrational modes: defected graphite, including heteroatom impurities (D1), disordered graphite lattice (D2), amorphous carbon (D3), hydrocarbon components (D4), and an ideal graphite structure (G) [18,45,46]. In the Raman spectrum of graphite, the low peak intensities of the D1 and D2 bands, the absence of the D3 and D4 bands, and the strong intensity of the G band are consistent with the typical Raman spectrum of well-ordered graphite. On the other hand, the increased peak intensities of the D1 to D4 bands can explain the elevated internal defects in the artificial graphene-based materials synthesized by arc discharge. The D1, D3, and D4 bands exhibit similar peak intensities in both UAG and NAG, but the D2 band shows a slightly higher peak intensity in NAG compared to UAG. Figure 1j shows the peak area ratio of the G band to the D2 band for each sample, and the graphene-based materials obtained by arc discharge display a significantly higher ratio of the D2 band compared to graphite. This indicates that nitrogen doping through arc discharge in the ideal graphite structure led to a notable presence of disordered graphitic lattice (D2). The weak intensity of the 2D peak in the UAG and NAG sample shown in Figure 1k is attributed to the formation of a turbostratic structure with weakly connected graphene layers due to N-doping.

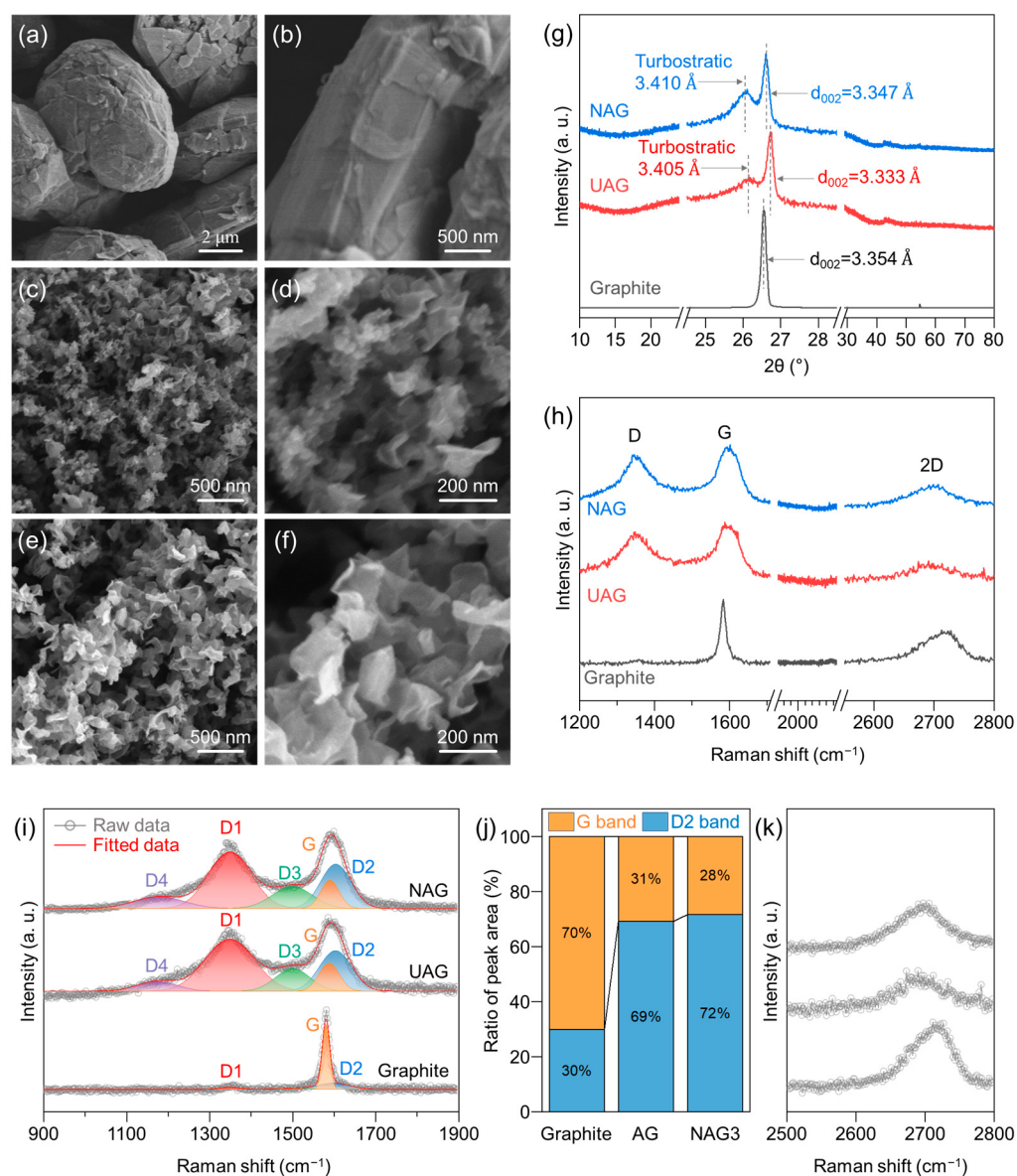


Figure 1. FE-SEM surface images: (a,b) graphite, (c,d) UAG, and (e,f) NAG samples, (b,d,f) images are magnified of (a,c,e) images. (g) XRD patterns and (h–k) Raman data for three samples: (h) Raman spectra, (i) deconvoluted spectra showing D1–D4, and G bands to investigate the disorder in the graphitic structure, (j) ratio of the peak area of the D2 band to the G band, and (k) magnified spectra highlighting the 2D band for graphite, UAG, and NAG.

Figure 2a–f displays the TEM results for UAG and NAG, respectively, synthesized via the arc-discharge method. Figure 2a,d present the high-resolution TEM cross-sectional images for the edge plane with numerous observed defects within the UAG and NAG structure, respectively. Additionally, these images show that both samples consist of graphene stacked in layers of six or more within a single sheet, which is consistent with the 2D band in the Raman spectra of both samples. The HR-TEM plane-view image in Figure 2b depicts the basal plane of non-overlapping graphene, revealing two sets of six-fold hexagonal spots rotated by 30° , which are characteristic of multi-layered graphene. The inset in Figure 2c displays the fast Fourier transform (FFT) of this basal plane image. This twisted graphene structure is further confirmed by the Moiré pattern in the inverse FFT (IFFT) image in Figure 2c. However, in other HR-TEM images of UAG beyond this section, the twist angles of the graphene layers were found to be randomly distributed, indicating no specific alignment of the twist angles (Figure S2). The analysis also revealed

that NAG exhibits a high density of defects and a twisted multilayer graphitic structure, as shown in Figure 2e,f.

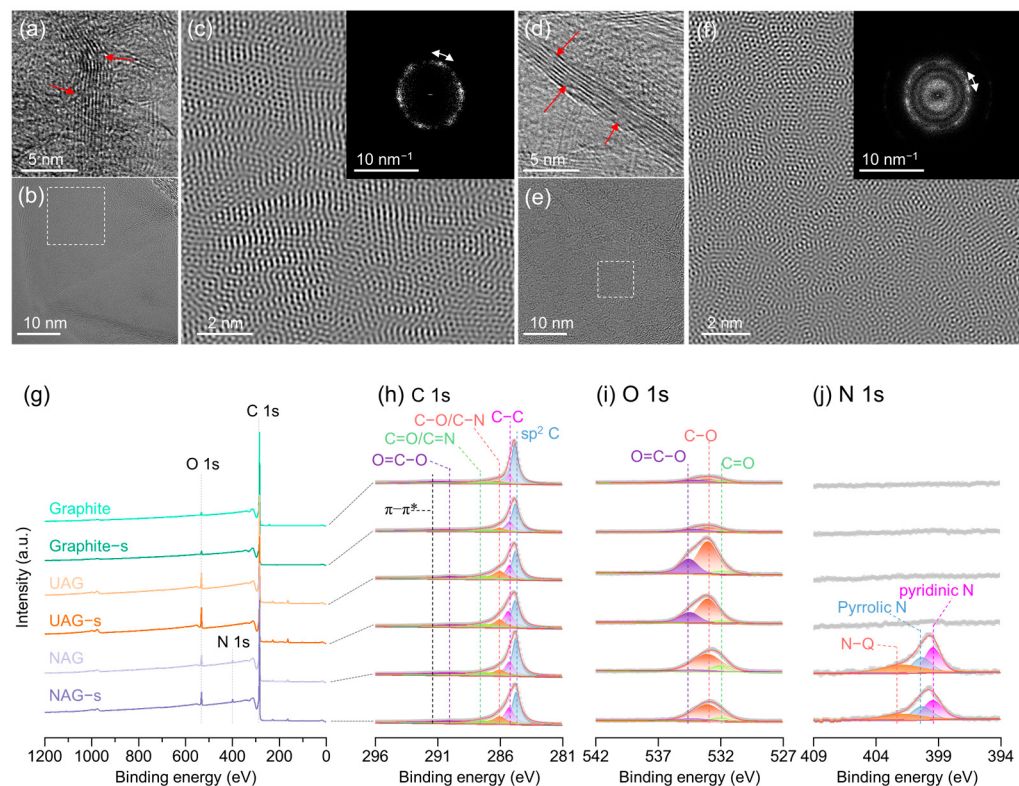


Figure 2. Transmission electron microscope (TEM) results of UAG: (a,b) high-resolution TEM image, (c) corresponding fast Fourier transform (FFT) image for the square dotted line of (b) [inset in Figure 2c] and inverse fast Fourier transform (IFFT) image. TEM results of NAG: (d,e) high-resolution TEM image, (f) corresponding FFT image for the square dotted line of (e) [inset in Figure 2f] and IFFT image. (The red arrows represent the defect sites.) XPS spectra of artificial graphite, UAG, and NAG samples before and after surface Ar⁺ sputtering (XPS spectra after sputtering were marked as ‘-s’): (g) survey-scan, (h) C 1s, (i) O 1s, and (j) N 1s, respectively.

The chemical composition and bonding configuration of graphene-based materials synthesized by the arc-discharge method were analyzed using XPS after surface sputtering by Ar⁺ and compared with those of artificial graphite, as shown in Figure 2g–j. In all three carbon materials, XPS spectra revealed core-level peaks at 285 eV (C 1s) and 533 eV (O 1s). Additionally, the NAG sample uniquely exhibited a core-level peak at 399 eV (N 1s). A detailed analysis of the C 1s core level showed a strong peak attributed to sp²-hybridized carbon. A deconvoluted peak at 291 eV was associated with delocalized π conjugation, contributing to the $\pi-\pi^*$ satellite feature [47,48]. The C 1s spectra of UAG and NAG were broader compared to that of graphite, with deconvolution revealing peaks centered at 284.7 eV for sp² carbon, at 285.3 eV for C–C bonding, at 286.0 eV for C–N or C–O bonding, at 287.1 eV for C=O/C=N bonding, and around 289.7 eV for O=C–O bonding, respectively. C 1s core-level analysis indicated that the concentration of sp² C was reduced, but the concentration of oxygen or nitrogen-bound carbon was higher in graphene-based material via arc discharge compared to graphite, as shown in Tables S3–S5. The higher oxygen- and nitrogen-related components in UAG and NAG induce structural disorder and numerous defects within the graphitic structure, thereby facilitating additional Na⁺ ion diffusion pathways. Notable differences were also observed in the O 1s and N 1s core levels, highlighting distinct characteristics between the two samples. The N 1s core-level spectrum of NAG exhibits distinct peaks corresponding to pyridinic N and pyrrolic N,

along with features associated with graphitic bonding at graphitic sites [43,49,50]. These are attributed to the formation of graphitic nitrogen (N-Q) during the heat treatment of PANI. The amount of nitrogen calculated from the peak area of each element is approximately 3.5%, which is relatively higher than that of the sample synthesized using NH₃ gas alone due to the addition of PANI [43]. As shown in Figure S3, the presence of pyrrolic N (31.8 at%) and pyridinic N (42.8 at%) contributes to the formation of defects within the graphene structure. Additionally, the relatively high content of graphitic N (25.4 at%) enhances the electrical conductivity of NAG, thereby improving its electronic properties, which are essential for efficient charge transport. This configuration is recognized as the most conductive form of nitrogen doping, facilitating rapid electron transport during electrochemical reactions. Impedance measurements of electrical conductivity revealed that the graphene-based material synthesized by arc discharge exhibited lower electrical resistance compared to graphite, as shown in Figure S4. Notably, NAG demonstrated slightly lower resistance than UAG, indicating enhanced conductivity characteristics and expected to be highly advantageous for high-rate charge/discharge applications.

Figure 3 presents the charge/discharge characteristics of graphite||Na, UAG||Na, and NAG||Na half-cells, measured to compare the sodium-ion storage capabilities of the ordered graphite structure with those of the turbostratic structure of the UAG and NAG. In Figure 3a, the initial charge/discharge profile of the graphite||Na half-cell exhibits the characteristic curve of Na-solvent co-intercalation, consistent with previous observations of sodium storage in graphite via solvent co-intercalation. In Figure 3b,c, the galvanostatic curves of UAG||Na and NAG||Na half-cells are very stable and exhibit higher specific capacity compared to the graphite||Na half-cell and the samples prepared with 1M NaPF₆ in ethylene carbonate/diethyl carbonate (1/1 by volume) with 10 wt% fluoroethylene carbonate electrolyte (Figure S5). In Figure 3d-f, CV curves were employed to investigate the voltage-current responses of graphite||Na, UAG||Na, and NAG||Na half-cells during their initial three cycles. In the first CV curve of graphite, the intercalation of Na-DEGDME and Faradaic reactions show prominent peaks at 0.53 V, with lower signals observed at 1.1, 0.73, and 0.2 V. In contrast, for UAG and NAG, the main Faradaic reactions are observed to be more prominent around 0.1 V compared to other potentials. During the first three CV cycles for both UAG and NAG, significant current peaks were observed at 0.65 V and 0.1 V in the cathodic and anodic scans, which are indicative of Na⁺-DEGDME co-intercalation and co-(de)intercalation. This behavior mirrors the sodium storage characteristics typically observed in graphite, suggesting that the sodium-ion storage mechanism in both arc-discharge graphene-based materials samples, which share a similar graphitic structure, is also driven by Na⁺-DEGDME co-intercalation [21,32,33]. All anodes (graphite, UAG, and NAG) exhibited stable cycling without any noticeable capacity degradation during charge/discharge cycling at a current density of 0.1 A g⁻¹, as shown in Figure 3g. After 50 cycles, the specific capacities of the graphite, UAG, and NAG anodes were 133.4, 181.9, and 163.6 mAh g⁻¹, respectively, demonstrating the relatively higher capacity of the arc-discharge graphene-based anode materials compared to the graphite anode. While graphite, UAG, and NAG exhibited stable cycling at low current densities, a difference in capacity retention emerged at the higher charge/discharge rate of 1 A g⁻¹, as shown in Figure 3h. For graphite, the specific capacity decreased from an initial 118 mAh g⁻¹ to 98.6 mAh g⁻¹ after 200 cycles, resulting in a capacity retention of 83.6%. This reduction is likely due to the limited sodium-ion diffusion within graphite, which causes side reactions under high current densities. Na⁺-solvent co-intercalation in graphite has shown high stability in DEGDME-based electrolytes, owing to their excellent anodic stability. However, at elevated current densities, the increased extent of Na⁺-solvent co-intercalation compromises the cycling stability of graphite anodes. In contrast, UAG and NAG main-

tained stable cycling performance at the same current density, with specific capacities of 137.9 mAh g^{-1} and 132.5 mAh g^{-1} after 200 cycles, respectively. Both samples exhibited nearly 100% capacity retention, indicating the superior cycling stability of arc-discharge graphene-based materials under high current conditions. In graphite's ordered structure, specific sodium-ion storage sites give rise to the characteristic bulk diffusion profile. In contrast, UAG and NAG possess a disordered turbostratic structure that provides numerous sodium diffusion pathways, enabling rapid sodium-ion storage due to shorter solid-state diffusion paths. This disordered structure likely enhances sodium-ion diffusion, supporting stable cycling performance even under high-rate conditions. The before (fresh samples) and after 200 cycles, the surface images of the samples are shown in Figures S6 and S7. Unlike UAG and NAG, graphite exhibits severe peeling. These results are consistent with the observation that, in the case of graphite, the capacity decreases during cycling at high current densities.

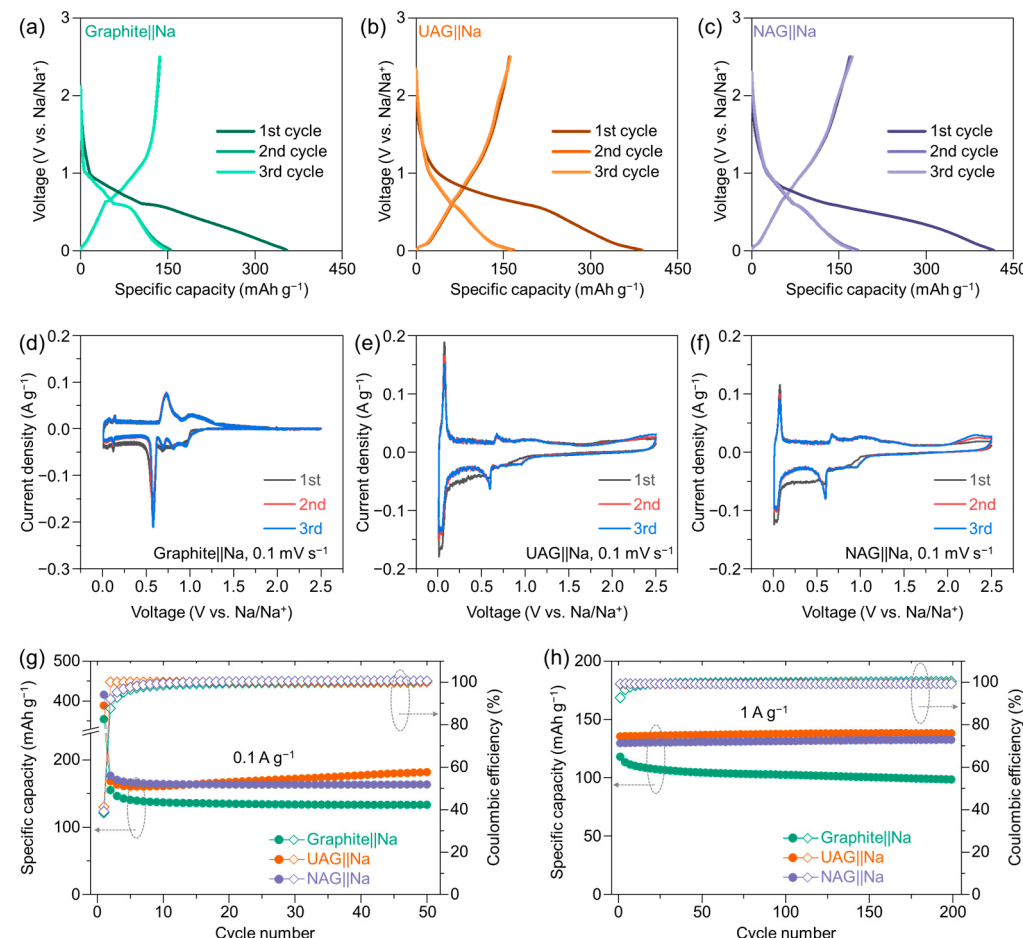


Figure 3. Electrochemical performances of the electrodes. (a–c) Galvanostatic charging/discharging plots during the initial three cycles for the three electrodes at a current density of 0.1 A g^{-1} : (a) graphite, (b) UAG, and (c) NAG. (d–f) Cyclic voltammetry curves during the initial three cycles for the three electrodes at a scan rate of 0.1 mV s^{-1} : (d) graphite, (e) UAG, and (f) NAG. (g,h) Cycling performance for graphite||Na, UAG||Na, and NAG||Na half-cells at (g) 0.1 and (h) 1 A g^{-1} .

Although the Na storage mechanism in UAG and NAG are similar to that of graphite, its co-intercalation kinetics are enhanced, resulting in faster charge/discharge rates. By examining the changes in current signals at different scan rates, as shown in Figure 4a–c, the Faradaic reaction rates for graphite, UAG, and NAG were analyzed using a power law [51,52]. Figure 4d–f displays the fitting results for $\log(\text{scan rate})$ vs. $\log(\text{peak current})$ for the cathodic (C1, C2) and anodic (A1, A2) peaks in AG, UAG, and NAG. The main Na

storage potential for the graphite active material is 0.54 V, which is higher compared to other peak intensities. The b values for UAG's A1, C1, A2, and A2 peaks were 0.82, 0.93, 0.90, and 0.98, respectively, while NAG showed values of 0.84, 0.91, 0.96, and 0.97, respectively. Both UAG and NAG exhibited b values approaching 1.0, indicating prominent capacitive behavior in their $i-v$ profiles. These high b values surpass those reported for natural graphite using the same ether-based DEGDME electrolyte, supporting the conclusion that arc-discharge synthesized turbostratic graphene-based materials demonstrate superior ion diffusion properties despite their relatively lower specific surface area. This observation is similar to previous research findings [53–55].

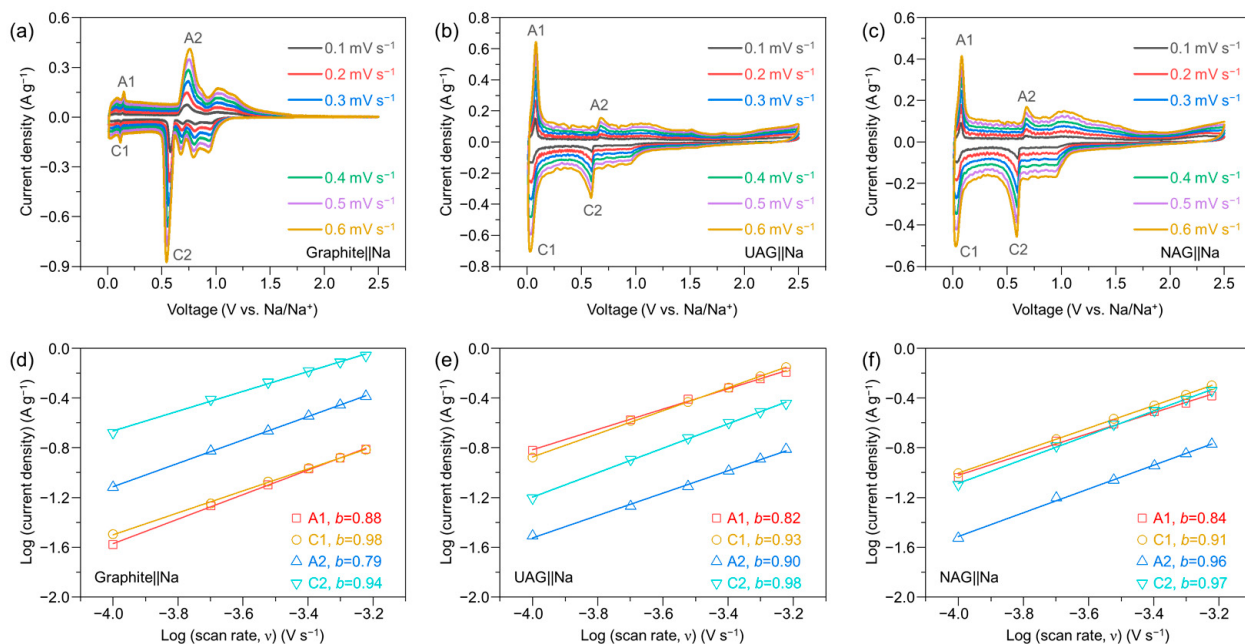


Figure 4. (a–c) CV curves at different scan rates and (d–f) log (scan rate) versus log (peak current) fitting plot for the two cathodic peaks (C1, and C2) and the two anodic peaks (A1, and A2) in graphite||Na, UAG||Na, and NAG||Na half-cells.

Figure 5 illustrates the comparison of the impedance component and the diffusion kinetics derived from the behavior of sodium ions in three anode materials, as shown by the in situ EIS and GITT results. Figure 5a,b show the detailed impedance values as a function of cell voltage during the first cycle obtained by in situ EIS for three electrodes displayed in Figure S8. As illustrated in Figure 5a, the resistance values of the three carbon-based anodes, specifically the series resistance (R_B) and charge transfer resistance (R_{ct}), exhibit a difference of approximately several ohms. The R_B , which reflects the combined effects of ion transport within the electrolyte and the intrinsic electrical resistance of the electrode, is notably lower for the graphite electrode than the UAG and NAG electrodes. This can be attributed to the slightly higher R_B values of UAG and NAG, which stem from their structural defects and the extended ionic transport pathways within the internal pore network in turbostratic structures [54,55]. These pathways result in a longer ionic diffusion distance, thereby increasing the overall ionic resistance. Conversely, the R_{ct} , which quantifies the charge transfer resistance at the electrode-electrolyte interface, is significantly lower for the UAG and NAG electrodes compared to graphite. This is primarily due to the increased number of defect sites and the porous structure of the turbostratic graphene-based materials, which facilitates a higher density of Faradaic reaction sites, thereby enhancing charge transfer kinetics. The fitting results of the Warburg impedance with respect to voltage in Figure S9 reveal a relatively higher diffusion coefficient for turbostratic graphene-based materials

compared to graphite, as shown in Figure 5b. In the voltage range of 1–3 V, UAG and NAG exhibit a diffusion coefficient of sodium ions (D_{Na^+}) approximately 10 times greater than that of graphite. This trend remains consistent even after the formation of the SEI during subsequent cycles.

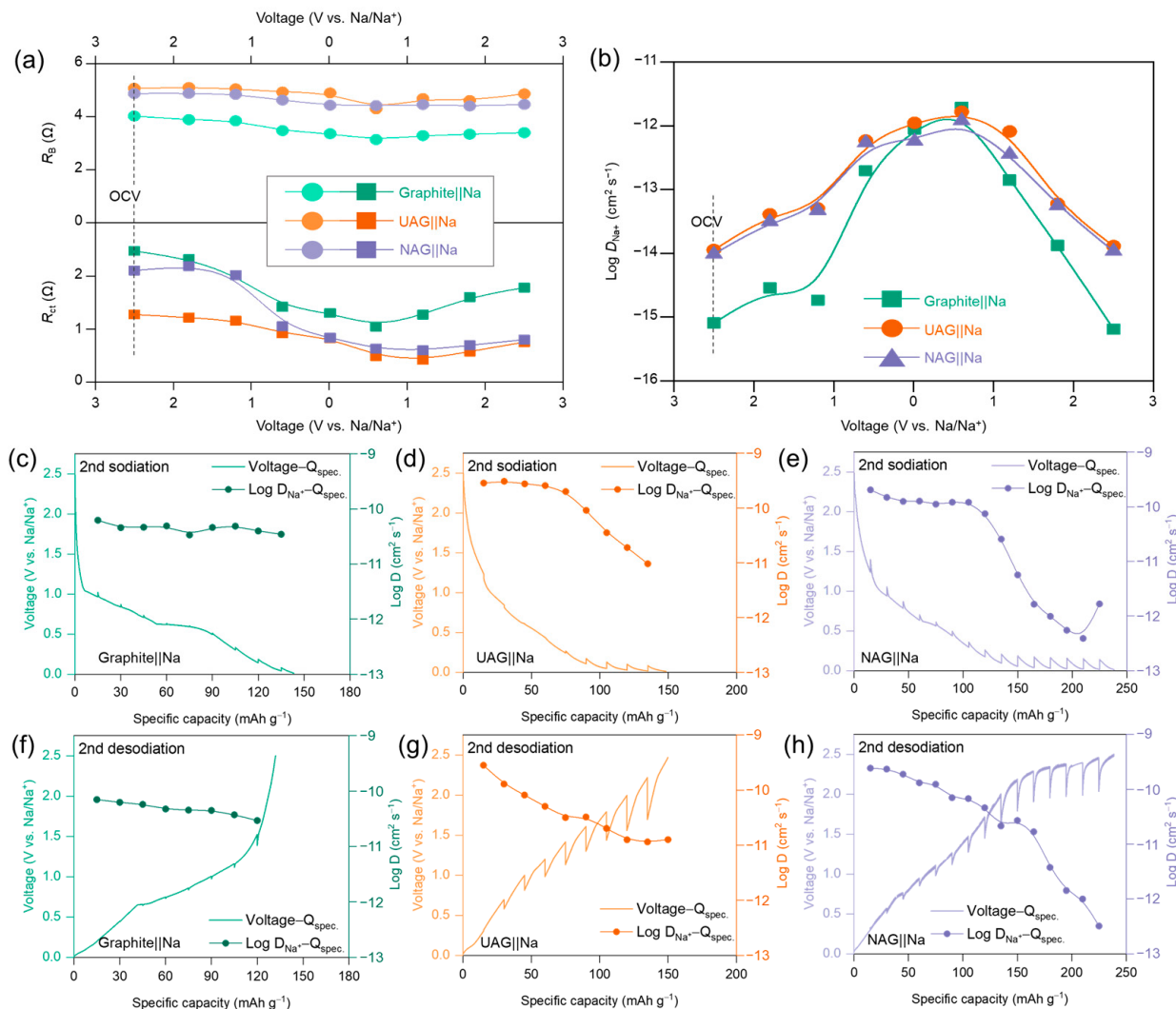


Figure 5. (a) The internal resistance values (R_B and R_{ct}) vs. voltage and (b) sodium ion diffusion coefficient (D_{Na^+}) were calculated from the EIS data for graphite||Na, UAG||Na, and NAG||Na half-cells at each voltage during the first cycle. GITT test and the calculated sodium ion diffusion coefficient (D_{Na^+}) during second cycles for the (c,f) graphite||Na, (d,g) UAG||Na, and (e,h) NAG||Na half-cells.

The rapid sodium storage kinetics of the turbostratic UAG and NAG are evident in the GITT measurement, as shown in Figure 5c–h. The applied current and voltage profiles to obtain GITT data, as well as the formula for calculating the D coefficient, are shown in Figure S10. In half-cells with three different carbon anodes and sodium, the D_{Na^+} values for graphite averaged $4.64 \times 10^{-11} \text{ S cm}^{-1}$, exhibiting consistent trends across the state-of-charge range. In contrast, the diffusion coefficients for UAG and NAG were approximately twice as high as that of graphite, with values of $2.62 \times 10^{-10} \text{ S cm}^{-1}$ and $1.77 \times 10^{-11} \text{ S cm}^{-1}$, respectively, during the slope regions of their voltage profiles. Notably, both UAG and NAG exhibit a plateau below 30 mV, where the diffusion coefficient decreases significantly. This decline in D_{Na^+} at a low potential is attributed to the sodium-ion charging mechanism, which transitions from intercalation to a pore-filling process, leading to the formation of

sodium clusters within the pores [56]. The pore-filling process, observed in GITT with pulse currents, is expected to occur in the numerous pores within the turbostratic structure of UAG and NAG, which are not exhibited in typical charge–discharge profiles with a 0.01 V cut-off voltage as shown in Figure 3e–f. The additional capacity through the pore-filling process in the GITT of UAG and NAG confirms the presence of numerous pores within the arc-discharge-synthesized turbostratic graphene-based materials, which contributes to enhanced ion diffusion.

Figure 6 illustrates the rate capability and high-current charge/discharge cycling performance of the prepared anode materials, assessed across a broad range of current densities to determine capacity retention under rapid charging/discharging conditions. In Figure 6a, current densities were systematically increased from 0.1 to 30 A g^{-1} and then reduced back to 0.1 A g^{-1} , allowing for a thorough evaluation of charge capacity at elevated current rates and the corresponding electrode stability under high-rate cycling. For the graphite||Na cell, charge capacities of 121.5, 105.2, 81.8, and 57.7 mAh g^{-1} were achieved at 0.1, 0.2, 0.5, and 1 A g^{-1} , respectively, demonstrating substantial capacity retention. However, above 2 A g^{-1} , capacity degradation was observed, likely due to increased diffusion overpotential, as the rate of electrochemical reactions became constrained by limited ion diffusion within the graphite structure. In contrast, the UAG||Na and NAG||Na cells exhibited robust high-rate performance even at elevated current densities, signifying a marked improvement in electrochemical behavior despite their relatively low specific surface areas. The UAG||Na and NAG||Na cells delivered specific capacities of 116.2, 112.4, 108.3, 104.6, 100.0, and 96.6 mAh g^{-1} at current densities of 0.1, 0.2, 0.5, 1, 2, and 3 A g^{-1} , respectively. Additionally, under equivalent conditions, NAG demonstrated slightly superior fast-charging capability compared to UAG, achieving specific capacities of 91.3, 81.3, 65.0, and 46.8 mAh g^{-1} at 5, 10, 20, and 30 A g^{-1} , respectively, compared to UAG's capacities of 88.9, 74.6, 55.6, and 36.7 mAh g^{-1} . Both materials retain their capacity even at high current densities, exhibiting exceptionally competitive performance relative to other graphene-based materials (Table S6). The specific capacity of NAG at 30 A g^{-1} is approximately 28% higher than that of UAG, which is a significant increase within the 3.5% nitrogen doping level. In Figure 6b, cycle stability at a high current density (5 A g^{-1}) for the artificial graphene-based materials was tested up to 2500 cycles. The specific capacities of NAG and UAG remained close to their initial values after 2500 cycles. In terms of long-term cycle stability, highly nitrogen-doped NAG demonstrated significantly higher capacity and Coulombic efficiency performance. Figure 6c visualizes the difference in sodium ion behavior of graphite and turbostratic graphene-based materials synthesized by arc discharge. In highly crystalline and well-ordered graphite, the solid-state diffusion of sodium ions is constrained to the crystallographic alignment. This anisotropic diffusion pathway imposes significant limitations under high current density conditions. The turbostratic graphene-based materials synthesized via the arc discharge method exhibit an extensive basal plane alongside abundant internal defects and sufficient porosity to facilitate electrolyte infiltration. This material also adopts a turbostratic structure, wherein the basal planes are twisted, introducing structural disorder and increased interlayer spacing. These intrinsic characteristics enable deep penetration of electrolytes into the active material particles and provide isotropic diffusion pathways for sodium ions through the defects, thereby supporting efficient ion transport under high current density conditions. Moreover, nitrogen doping, including pyrrolic, pyridinic, and graphitic nitrogen, was readily induced through the arc discharge method. The incorporation of these nitrogen species contributed to a modest enhancement in electrochemical performance, as reflected in the improved material characteristics.

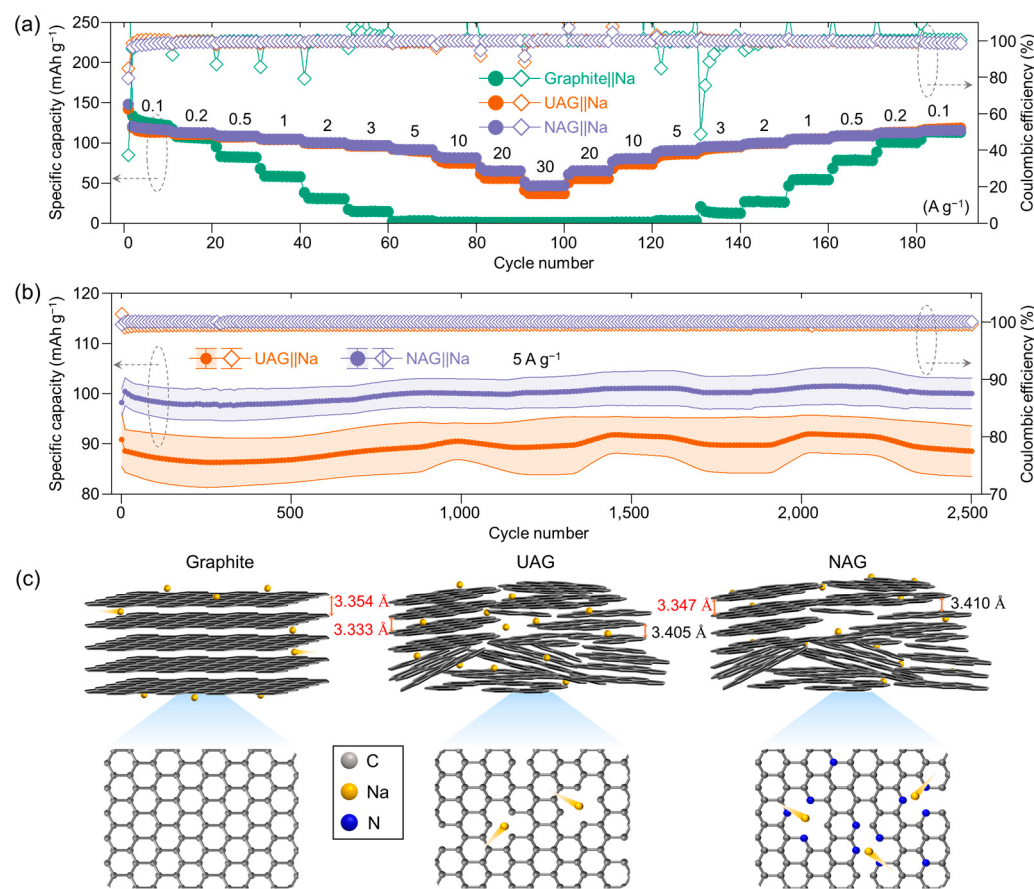


Figure 6. (a) Rate capability of graphite||Na, UAG||Na, and NAG||Na half-cells at current densities ranging from 0.1 to 30 A g^{-1} , and then back to 0.1 A g^{-1} . (b) Long cycle stability of UAG||Na and NAG||Na half-cells at 5 A g^{-1} . (c) Schematic of Na^+ ion kinetics for the samples at high current density during cycling.

4. Conclusions

In summary, high N-doped ($\sim 3.5\%$) artificial graphene-based material has been synthesized through the PANI-based arc-discharge method for sodium-ion battery anodes. Broad peaks, except for the main graphite peak, are observed at 26.2° [$d_{ts} = 3.405\text{ \AA}$] for UAG and 26.1° [$d_{ts} = 3.410\text{ \AA}$] for NAG, characteristic of a typical turbostratic graphene structure. In turbo-structural graphene, doping with nitrogen increases structural disordering, improves electronic conductivity, and enhances the diffusion of Na^+ ions through defects and pores, enabling fast charging and discharging kinetics. The NAG anode demonstrates long-cycle stability and high-rate capability. At low current densities, there was little difference in the behavior of Na^+ ions and charge transfer between UAG and NAG, but as the current density increased, the role of nitrogen became more pronounced, and the two samples showed a significant difference compared to graphite. The NAG electrode, produced via a facile and scalable physical arc discharge method, exhibits significant potential as an anode material for sodium-ion batteries. Notably, it demonstrates promising applicability in configurations demanding rapid charge and discharge capabilities.

Supplementary Materials: The following supporting information can be downloaded at <https://www.mdpi.com/article/10.3390/batteries11040135/s1>; Figure S1: Schematic illustration of arc-discharge system for synthesis of UAG and NAG; Figure S2: HR-TEM results of UAG. (a) UAG observed along the edge plane direction, (b) non-overlapped single UAG layer observed along the basal plane direction, (c) IFFT image of the highlighted region in (b) (inset: corresponding FFT image); Figure S3: Elemental composition (C, O, N, and impurity) in the graphite, UAG, and NAG determined by XPS

spectra. Inset shows the contents of deconvoluted nitrogen component, pyridinic N, pyrrolic N, and graphitic N. Figure S4: (a) Illustration of the configuration to test electrical conductivity (stainless steel-symmetric pressure cell), and (b) corresponding equivalent circuit. (c) Nyquist plots for SS||SS for graphite, UAG, and NAG. (d) Calculated resistivity of graphite, UAG, and NAG; Figure S5: (a,b) Galvanostatic charging/discharging profiles for UAG||Na and NAG||Na half-cells, respectively, using a carbonate-based electrolyte of 1M NaPF₆ in ethylene carbonate/diethyl carbonate (EC/DEC, 1/1 by volume) with 10 wt% fluoroethylene carbonate (FEC); Figure S6: Plan-view FE-SEM images of (a,b) the fresh graphite anode, (c,d) the fresh UAG anode, and (e,f) the fresh NAG anode before cycling; Figure S7: Plan-view FE-SEM images of (a,b) the cycled graphite anode, (c,d) the cycled UAG anode, and (e,f) the cycled NAG anode after galvanostatic charging/discharging cycling at the current density of 1 A g⁻¹ for 200 cycles; Figure S8: In situ EIS results for (a,d) graphite||Na, (b,e) UAG||Na, and (c,f) NAG||Na half cells at different potential. (a–c) Charging and discharging curves during the in situ EIS measurement (marked circles are represented as the measured point of EIS). (d–f) Nyquist plots at different potentials; Figure S9: (a–c) Z_{re} vs. $\omega^{-1/2}$ and (d–f) slope of Z_{re} vs. $\omega^{-1/2}$ as a function of voltage obtained from in situ EIS results of the Figure S5; Figure S10: Applied current pulse to the samples and the corresponding voltage profile used to obtain GITT data.; Figure S11: Galvanostatic charging/discharging curves at different current densities from 0.1 A g⁻¹ to 5.0 A g⁻¹ for (a) UAG||Na, and (b) NAG||Na; Table S1: Deconvoluted peak information in XRD spectra for graphite, UAG, and NAG by deconvoluting to graphitic carbon (g-C) and turbostratic carbon (t-C); Table S2: Deconvoluted peak information in Raman spectra for graphite, UAG, and NAG; Table S3: Deconvoluted peak information in XPS spectra of C 1s core level for graphite, UAG, and NAG; Table S4: Deconvoluted peak information in XPS spectra of O 1s core level for graphite, UAG, and NAG; Table S5: Deconvoluted peak information in XPS spectra of N 1s core level for NAG; Table S6: Comparison table on the electrochemical performance of graphene and graphene-related compound for SIB's anode.

Author Contributions: Conceptualization, I.J., M.J.K. and C.-R.C.; methodology, I.J. and C.K.; validation, M.K., H.W.K., H.C. and H.S.Y.; formal analysis, I.J., M.K., H.W.K. and H.S.Y.; investigation, I.J. and C.K.; resources, M.K., H.W.K., H.C. and H.S.Y.; data curation, I.J.; writing—original draft preparation, I.J., H.C. and C.-R.C.; writing—review and editing, I.J., H.C. and C.-R.C.; visualization, I.J., and H.S.Y.; supervision, M.J.K. and C.-R.C.; project administration, C.-R.C.; funding acquisition, C.-R.C. All authors have read and agreed to the published version of the manuscript.

Funding: This work was supported by a 2-Year Research Grant of Pusan National University.

Data Availability Statement: The data presented in this study are available from the corresponding author on request.

Conflicts of Interest: The authors declare no conflicts of interest.

Abbreviations

The following abbreviations are used in this manuscript:

UAG	Undoped artificial graphene-based material
NAG	Nitrogen-doped artificial graphene-based material
LIBs	Lithium-ion batteries
SIBs	Sodium-ion batteries
PANI	Polyaniline
FE-SEM	Field-emission scanning electron microscopy
HR-TEM	High-resolution transmission electron microscopy
XRD	X-ray diffraction
XPS	X-ray photoelectron spectroscopy
DEGDME	Diethylene glycol dimethyl ether
SBR	Styrene butadiene rubber
CMC	Carboxymethyl cellulose

CV	Cyclic voltammetry
GITT	Galvanostatic intermittent titration technique
EIS	Electrochemical impedance spectroscopy
FFT	Fast Fourier transform
IFFT	Inverse fast Fourier transform

References

1. Liu, B.; Zhang, Z.D.; Xu, X. Advancing Lithium Metal Batteries. *Joule* **2018**, *2*, 833–845. [[CrossRef](#)]
2. Liu, J.; Bao, Z.; Cui, Y.; Dufek, E.J.; Goodenough, J.B.; Khalifah, P.; Li, Q.; Liaw, B.Y.; Liu, P.; Manthiram, A.; et al. Pathways for practical high-energy long-cycling lithium metal batteries. *Nat. Energy* **2019**, *4*, 180–186. [[CrossRef](#)]
3. Schmuck, R.; Wagner, R.; Hörpel, G.; Placke, T.; Winter, M. Performance and cost of materials for lithium-based rechargeable automotive batteries. *Nat. Energy* **2018**, *3*, 267–278.
4. Abraham, K.M. How Comparable Are Sodium-Ion Batteries to Lithium-Ion Counterparts? *ACS Energy Lett.* **2020**, *5*, 3544–3547.
5. Gupta, P.; Pushpakant, S.; Haider, M.A.; Basu, S. Understanding the Design of Cathode Materials for Na-Ion Batteries. *ACS Omega* **2022**, *7*, 5605–5614. [[PubMed](#)]
6. Nayak, P.K.; Yang, L.; Brehm, W.; Adelhelm, P. From Lithium-Ion to Sodium-Ion Batteries: Advantages, Challenges, and Surprises. *Angew. Chem. Int. Ed. Engl.* **2018**, *57*, 102–120.
7. Masese, T.; Yoshii, K.; Yamaguchi, Y.; Okumura, T.; Huang, Z.D.; Kato, M.; Kubota, K.; Furutani, J.; Orikasa, Y.; Senoh, H.; et al. Rechargeable potassium-ion batteries with honeycomb-layered tellurates as high voltage cathodes and fast potassium-ion conductors. *Nat. Commun.* **2018**, *9*, 3823.
8. Liu, Y.; Tai, Z.; Zhang, J.; Pang, W.K.; Zhang, Q.; Feng, H.; Konstantinov, K.; Guo, Z.; Liu, H.K. Boosting potassium-ion batteries by few-layered composite anodes prepared via solution-triggered one-step shear exfoliation. *Nat. Commun.* **2018**, *9*, 3645.
9. Lin, M.C.; Gong, M.; Lu, B.; Wu, Y.; Wang, D.Y.; Guan, M.; Angell, M.; Chen, C.; Yang, J.; Hwang, B.J.; et al. An ultrafast rechargeable aluminium-ion battery. *Nature* **2015**, *520*, 325–328.
10. Wang, N.; Wan, H.; Duan, J.; Wang, X.; Tao, L.; Zhang, J.; Wang, H. A review of zinc-based battery from alkaline to acid. *Mater. Today Adv.* **2021**, *11*, 100149. [[CrossRef](#)]
11. Vaalma, C.; Buchholz, D.; Weil, M.; Passerini, S. A cost and resource analysis of sodium-ion batteries. *Nat. Rev. Mater.* **2018**, *3*, 1–11.
12. Yabuuchi, N.; Kubota, K.; Dahbi, M.; Komaba, S. Research Development on Sodium-Ion Batteries. *Chem. Rev.* **2014**, *114*, 11636–11682. [[PubMed](#)]
13. Cohn, A.P.; Muralidharan, N.; Carter, R.; Share, K.; Pint, C.L. Anode-Free Sodium Battery through in Situ Plating of Sodium Metal. *Nano Lett.* **2017**, *17*, 1296–1301.
14. Zhang, W.; Zhang, F.; Ming, F.; Alshareef, H.N. Sodium-ion battery anodes: Status and future trends. *Energy Chem.* **2019**, *1*, 100012.
15. Lv, J.; Wang, Q.; OuYang, M.; Cao, Y. Highly Performing Sodium Metal Batteries Reinforced by a Self-Regulated Dual-Layered Solid Electrolyte Interphase via a Metal–Organic Framework. *ACS Appl. Mater. Interfaces* **2024**, *16*, 41570–41582. [[PubMed](#)]
16. Wang, X.; Zhang, C.; Sawczyk, M.; Sun, J.; Yuan, Q.; Chen, F.; Mendes, T.C.; Howlett, P.C.; Fu, C.; Wang, Y.; et al. Ultra-stable all-solid-state sodium metal batteries enabled by perfluoropolyether-based electrolytes. *Nat. Mater.* **2022**, *21*, 1057–1065.
17. Jeon, I.; Yang, D.; Yadav, D.; Seo, J.; Zhang, H.; Yin, L.; Ahn, H.S.; Cho, C.R. Sodium storage behavior and long cycle stability of boron-doped carbon nanofibers for sodium-ion battery anodes. *Electrochim. Acta* **2023**, *439*, 141730.
18. Jeon, I.; Kim, T.; Seo, J.; Jeong, I.K.; Lee, J.H.; Park, M.; Park, Y.; Yang, D.; Cho, C.R. Enhanced electrochemical performance and interdiffusion behavior of sodium ions in onion-derived freeze-dried and KOH-activated carbon for sodium-ion battery anodes. *Appl. Surf. Sci.* **2024**, *648*, 159023.
19. Xiao, L.; Lu, H.; Fang, Y.; Sushko, M.L.; Cao, Y.; Ai, X.; Yang, H.; Liu, J. Low-Defect and Low-Porosity Hard Carbon with High Coulombic Efficiency and High Capacity for Practical Sodium Ion Battery Anode. *Adv. Energy Mater.* **2018**, *8*, 1703238.
20. Alvin, S.; Yoon, D.; Chandra, C.; Cahyadi, H.S.; Park, J.H.; Chang, W.; Chung, K.Y.; Kim, J. Revealing sodium ion storage mechanism in hard carbon. *Carbon* **2019**, *145*, 67–81.
21. Jache, B.; Adelhelm, P. Use of Graphite as a Highly Reversible Electrode with Superior Cycle Life for Sodium-Ion Batteries by Making Use of Co-Intercalation Phenomena. *Angew. Chem. Int. Ed. Engl.* **2014**, *53*, 10169–10173. [[PubMed](#)]
22. Zhang, N.; Han, X.; Liu, Y.; Hu, X.; Zhao, Q.; Chen, J. 3D Porous γ -Fe₂O₃ @C Nanocomposite as High-Performance Anode Material of Na-Ion Batteries. *Adv. Energy Mater.* **2014**, *5*, 1401123.
23. Naeyaert, P.J.P.; Avdeev, M.; Sharma, N.; Yahia, H.B.; Ling, C.D. Synthetic, Structural, and Electrochemical Study of Monoclinic Na₄Ti₅O₁₂ as a Sodium-Ion Battery Anode Material. *Chem. Mater.* **2014**, *26*, 7067–7072.

24. Ma, D.; Li, Y.; Mi, H.; Luo, S.; Zhang, P.; Lin, Z.; Li, J.; Zhang, H. Robust SnO₂@x Nanoparticle-Impregnated Carbon Nanofibers with Outstanding Electrochemical Performance for Advanced Sodium-Ion Batteries. *Angew. Chem. Int. Ed. Engl.* **2018**, *57*, 8901–8905. [PubMed]
25. Wang, L.; Wei, Z.; Mao, M.; Wang, H.; Li, Y.; Ma, J. Metal oxide/graphene composite anode materials for sodium-ion batteries. *Energy Storage Mater.* **2019**, *16*, 434–454.
26. Zhao, W.; Ma, X.; Wang, X.; Zhou, H.; He, X.; Yao, Y.; Ren, Y.; Luo, Y.; Zheng, D.; Sun, S.; et al. Synergistically Coupling Atomic-Level Defect-Manipulation and Nanoscopic-Level Interfacial Engineering Enables Fast and Durable Sodium Storage. *Small* **2024**, *20*, 2311055. [CrossRef]
27. Vincent, M.; Kumar, S.S.; Kowalski, D. Pseudocapacitive vs. diffusion controlled charge storage in Fe₂O₃ nanosheet Na-ion battery. *Electrochim. Acta* **2023**, *469*, 143161.
28. Fang, Y.; Luan, D.; Lou, X.W.D. Recent Advances on Mixed Metal Sulfides for Advanced Sodium-Ion Batteries. *Adv. Mater.* **2020**, *32*, e2002976.
29. Xiao, Y.; Lee, S.H.; Sun, Y.K. The Application of Metal Sulfides in Sodium Ion Batteries. *Adv. Energy Mater.* **2016**, *7*, 1601329.
30. Yang, D.; Yadav, D.; Jeon, I.; Seo, J.; Jeong, S.Y.; Cho, C.R. Enhanced High-Rate Capability and Long Cycle Stability of FeS@NCG Nanofibers for Sodium-Ion Battery Anodes. *ACS Appl. Mater. Interfaces* **2022**, *14*, 44303–44316.
31. Han, B.; Zou, Y.; Xu, G.; Hu, S.; Kang, Y.; Qian, Y.; Wu, J.; Ma, X.; Yao, J.; Li, T.; et al. Additive stabilization of SEI on graphite observed using cryo-electron microscopy. *Energy Environ. Sci.* **2021**, *14*, 4882–4889.
32. Kim, H.; Hong, J.; Park, Y.U.; Kim, J.; Hwang, I.; Kang, K. Sodium Storage Behavior in Natural Graphite using Ether-based Electrolyte Systems. *Adv. Funct. Mater.* **2014**, *25*, 534–541.
33. Xu, Z.L.; Yoon, G.; Park, K.Y.; Park, H.; Tamwattana, O.; Kim, S.J.; Seong, W.M.; Kang, K. Tailoring sodium intercalation in graphite for high energy and power sodium ion batteries. *Nat. Commun.* **2019**, *10*, 2598. [PubMed]
34. Zhu, J.; Chen, C.; Lu, Y.; Ge, Y.; Jiang, H.; Fu, K.; Zhang, X. Nitrogen-doped carbon nanofibers derived from polyacrylonitrile for use as anode material in sodium-ion batteries. *Carbon* **2015**, *94*, 189–195.
35. Cao, Y.; Xiao, L.; Sushko, M.L.; Wang, W.; Schwenzer, B.; Xiao, J.; Nie, Z.; Saraf, L.V.; Yang, Z.; Liu, J. Sodium ion insertion in hollow carbon nanowires for battery applications. *Nano Lett.* **2012**, *12*, 3783–3787.
36. Tian, Y.; Yang, H.; Zeng, Y.; Qi, Y.; Wang, W.; Chen, H.; Yin, W.; Ke, Y.; Jian, Z.; Kan, W.H.; et al. Design of High-Performance Defective Graphite-Type Anodes for Sodium-Ion Batteries. *ACS Appl. Energy Mater.* **2023**, *6*, 3854–3861.
37. Zhou, L.F.; Wang, Y.S.; Jia, H.; Gong, H.; Liu, L.Y.; Du, T. Application of rich-defect expanded graphite with improved ion transport and kinetics for sodium storage at low temperature. *Sustain. Energy Fuels* **2022**, *6*, 1727–1732.
38. Wang, P.; Zhu, X.; Wang, Q.; Xu, X.; Zhou, X.; Bao, J. Kelp-derived hard carbons as advanced anode materials for sodium-ion batteries. *J. Mater. Chem. A* **2017**, *5*, 5761–5769.
39. Kumar, S.S.A.; Badawi, M.N.; Liew, J.; Prasankumar, T.; Ramesh, K.; Ramesh, S.; Tiong, S.K. High-Performance Sodium-Ion Batteries with Graphene: An Overview of Recent Developments and Design. *ChemSusChem* **2025**, *14*, e202400958.
40. Sun, Z.; Wang, Y.; Jiang, X.; Bando, Y.; Wang, X. 3D network of graphene materials for alkali metal ion batteries. *EnergyChem* **2025**, *7*, 100149. [CrossRef]
41. Wen, P.; Sun, Z.; Li, Y.; Shi, X.; Huang, H.; Lu, P.; Qin, J.; Li, Y.; Yin, Q.; Yang, X.; et al. Atomic indium decorated graphene for dendrite-free sodium anodes towards high-energy-density sodium-metal batteries. *J. Energy Chem.* **2025**, *104*, 44–51.
42. Guo, R.; Lv, C.; Xu, W.; Sun, J.; Zhu, Y.; Yang, X.; Li, J.; Sun, J.; Zhang, L.; Yang, D. Effect of Intrinsic Defects of Carbon Materials on the Sodium Storage Performance. *Adv. Energy Mater.* **2020**, *10*, 1903652.
43. Pham, T.V.; Kim, J.G.; Jung, J.Y.; Kim, J.H.; Cho, H.; Seo, T.H.; Lee, H.; Kim, N.D.; Kim, M.J. High areal capacitance of N-doped graphene synthesized by arc discharge. *Adv. Funct. Mater.* **2019**, *29*, 1905511.
44. Kim, C.; Kim, J.-G.; Kim, N.D.; Kim, M.J. Arc discharge synthesis of graphene with enhanced boron doping concentration for electrochemical applications. *Appl. Surf. Sci.* **2023**, *637*, 157825.
45. Sadezky, A.; Muckenhuber, H.; Grothe, H.; Niessner, R.; Pöschl, U. Raman microspectroscopy of soot and related carbonaceous materials: Spectral analysis and structural information. *Carbon* **2005**, *43*, 1731–1742.
46. Quan, Z.; Wang, F.; Wang, Y.; Liu, Z.; Zhang, C.; Qi, F.; Zhang, M.; Ye, C.; Tan, J.; Liu, J. Robust Micro-Sized and Defect-Rich Carbon–Carbon Composites as Advanced Anodes for Potassium-Ion Batteries. *Small* **2024**, *20*, 2305841.
47. Blume, R.; Rosenthal, D.; Tessonner, J.P.; Li, H.; Knop-Gericke, A.; Schlögl, R. Characterizing graphitic carbon with X-ray photoelectron spectroscopy: A step-by-step approach. *ChemCatChem* **2015**, *7*, 2871–2881.
48. Cabello, M.; Bai, X.; Chyrka, T.; Ortiz, G.F.; Lavela, P.; Alcantara, R.; Tirado, J.L. On the reliability of sodium co-intercalation in expanded graphite prepared by different methods as anodes for sodium-ion batteries. *J. Electrochem. Soc.* **2017**, *164*, A3804.
49. Kondo, T.; Guo, D.; Shikano, T.; Suzuki, T.; Sakurai, M.; Okada, S.; Nakamura, J. Observation of Landau levels on nitrogen-doped flat graphite surfaces without external magnetic fields. *Sci. Rep.* **2015**, *5*, 16412.
50. Wu, J.; Yadav, R.M.; Yang, Y.; Zhang, X.; Vajtai, R.; Lou, J.; Ajayan, P.M. Nitrogen-Doped Graphene with Pyridinic Dominance as a Highly Active and Stable Electrocatalyst for Oxygen Reduction. *ACS Appl. Mater. Interfaces* **2015**, *7*, 14763–14769.

51. Kim, T.; Choi, W.; Shin, H.C.; Choi, J.Y.; Kim, J.M.; Park, M.S.; Yoon, W.S. Applications of voltammetry in lithium ion battery research. *J. Electrochem. Sci. Technol.* **2020**, *11*, 14–25.
52. Yang, X.; Rogach, A.L. Electrochemical techniques in battery research: A tutorial for nonelectrochemists. *Adv. Energy Mater.* **2019**, *9*, 1900747.
53. Cheng, D.; Zhou, X.; Hu, H.; Li, Z.; Chen, J.; Miao, L.; Ye, X.; Zhang, H. Electrochemical storage mechanism of sodium in carbon materials: A study from soft carbon to hard carbon. *Carbon* **2021**, *182*, 758–769.
54. Luo, S.; Liu, F.; Tianxu, W.; Liu, Y.; Zhang, C.; Bie, C.; Liu, M.; Chu, P.K.; Huo, K.; Gao, B. Regeneration of spent graphite via graphite-like turbostratic carbon coating for advanced Li ion battery anode. *Energy Storage Mater.* **2024**, *73*, 103833.
55. Wang, D.; Lian, J.; Wang, Y.; Jia, P.; Gao, F. Turbostratic Lattice and Electronegativity Modification Jointly Enabled an Ultra-High-Rate and Long-Lived Carbon Anode for Potassium-Ion Batteries. *ACS Appl. Mater. Interfaces* **2023**, *15*, 15585–15594.
56. Aniskevich, Y.; Yu, J.H.; Kim, J.-Y.; Komaba, S.; Myung, S.-T. Tracking Sodium Cluster Dynamics in Hard Carbon with a Low Specific Surface Area for Sodium-Ion Batteries. *Adv. Energy Mater.* **2024**, *14*, 2304300. [[CrossRef](#)]

Disclaimer/Publisher’s Note: The statements, opinions and data contained in all publications are solely those of the individual author(s) and contributor(s) and not of MDPI and/or the editor(s). MDPI and/or the editor(s) disclaim responsibility for any injury to people or property resulting from any ideas, methods, instructions or products referred to in the content.